Electronic Supplementary Material (ESI) for Journal of Materials Chemistry A.
This journal is © The Royal Society of Chemistry 2023

Heterostructured MoP/$CoMoP_2$ embedded in N, P-doped carbon matrix as a highly efficient cooperative catalyst for pH-universal overall water splitting

Luyao Zheng[a, b], Cong Liu[c], Wenbiao Zhang[a, d], Boxu Gao[a], Tianlan Yan[a], Yahong Zhang[a], Xiaoming Cao[c], Qingsheng Gao[c*] and Yi Tang[a*]

a. Department of Chemistry, Shanghai Key Laboratory of Molecular Catalysis and Innovative Materials, Laboratory of Advanced Materials and Collaborative Innovation Center of Chemistry for Energy Materials, Fudan University, Shanghai 200433, China. E-mail: yitang@fudan.edu.cn

b. School of Materials Science and Engineering, Changzhou Key Laboratory of Intelligent Manufacturing and Advanced Technology for Power Battery, Changzhou University, Changzhou 213164, China.

c. Key Laboratory for Advanced Materials, Center for Computational Chemistry and Research Institute of Industrial Catalysis, School of Chemistry and Molecular Engineering, East China University of Science & Technology, Shanghai 200237, China.

d. College of Chemistry and Materials Science, And Guangdong Provincial Key Laboratory of Functional Supramolecular Coordination Materials and Applications, Jinan University, Guangzhou, 510632, China. E-mail: tqsgao@jnu.edu.cn

Electrochemical measurements

Hydrogen evolution reaction (HER) and oxygen evolution reactions (OER) were conducted at room temperature using a typical three-electrode configuration equipped with a CHI760E potentiostat (CH Instruments, China). All the potentials were converted to this reversible hydrogen electrode (RHE) according to the equation:

$$E(RHE) = E(SCE) + 0.2422 + 0.059pH, in\ acidic\ or\ neutral\ \ media \quad (1)$$

$$E(RHE) = E\left(\frac{Hg}{HgO}\right) + 0.098 + 0.059pH, in\ alkaline\ media \quad (2)$$

Overall water splitting (OWS) was conducted using a typical two-electrode system. The working electrode modified by catalysts was prepared as following procedure. 20 mg of the catalysts were ultrasonicated with 1 mL of water-ethanol-nafion solution with V_{water}: $V_{ethanol}$: $V_{nafion\ solution}$=7:2:1 for 30 min to obtain a homogeneous ink. Then, 4 μL of the as-prepared ink was coated onto the glassy carbon electrode and dried in air. Linear sweep voltammetry (LSV) was performed in 0.5 M H_2SO_4, 1 M KOH or 1.0 M phosphate buffered saline (PBS) at a scan rate of 5 mV s^{-1} with IR-corrections conducted for every electrode. A saturated calomel electrode (in 0.5 M H_2SO_4 or 1.0 M PBS) or Hg/HgO (in 1 M KOH) electrode was acting as the reference electrode and graphite rod as counter electrode. Cyclic voltammograms (CV) test was performed from 0 to 0.3 V (versus RHE) with different scan rates (25, 50, 75, 100, 150, 200, 250 and 300 mV s^{-1}). Electrochemical impedance spectroscopy (EIS) was conducted at 200 mV (versus RHE) from 10^{-2} to 10^{6} Hz.

EXAFS fitting

Data reduction, data analysis, and EXAFS fitting were performed and analyzed with the Athena and Artemis programs of the Demeter data analysis packages (reference 1) that utilizes the FEFF6 program (reference 3) to fit the EXAFS data. The energy calibration of the sample was conducted through standard Co foil and Mo foil, which as a reference was simultaneously measured. A linear function was subtracted from the pre-edge region, then the edge jump was normalized using Athena software. The *χ(k)* data were isolated by subtracting a smooth, third-order polynomial approximating the absorption background of an isolated atom. The *k3*-weighted *χ(k)* data were Fourier

transformed after applying a Hanning window function (Δk = 1.0). For EXAFS modeling, the global amplitude EXAFS (*CN, R,* σ^2 and ΔE_0) were obtained by nonlinear fitting, with least-squares refinement, of the EXAFS equation to the Fourier-transformed data in *R*-space, using Artemis software, EXAFS of the Co foil and Mo foil are fitted and the obtained amplitude reduction factor S_0^2 value (0.791 and 0.946) was set in the EXAFS analysis to determine the coordination numbers (*CNs*) in the Co/Mo-O scattering path in sample.

The TOF calculation

we assume that all Mo and Co atoms of electrocatalyst are active sites and the Faraday efficiency is 100%.

$$\text{TOF} = \frac{\text{the number of theoretic Hydrogen molecules } (n_{H_2})}{\text{the total number of Mo } and\ Co \text{ atoms on the electrode } (n_{MoCo})}$$

$$n_{MoCo} = \left(\frac{m_{loading} \times W_{Mo}}{M_{Mo}} + \frac{m_{loading} \times W_{Co}}{M_{Co}}\right) \times N_A$$

$$n_{H_2} = \frac{j_\eta \times S \times N_A}{n \times F}$$

Where $m_{loading}$ is the loading mass of the catalysts on the surface of glass carbon; W_{Mo} and W_{Co} are the content of Mo and Co element collected by ICP; M_{Mo} and M_{Co} are relative atomic masses of Co and Mo; N_A is the Avogadro's number (6.02×10^{23} mol^{-1}); j_η is the current density at an overpotential of η; S is the surface area of glassy carbon electrode; n is the number of electrons transferred per molecule (2 for HER); F is the Faraday constant (96485 C mol^{-1}).

Density Functional Theory Calculations

All calculations were performed with the Perdew–Burke–Ernzerhof (PBE) functional using the VASP code. Standard projector-augmented-wave (PAW) method was used to represent the core-valence electron interaction. PBE-D3 (BJ) is also included to describe van der Waals interaction. The valence electronic states were expanded in plane wave basis sets with energy cutoff of 450 eV.

The $CoMoP_2$ (104) surface is modeled by a 5-layer p(1 × 3) unit cell of 15.8 Å, 9.8 Å with a 20.0 Å vacuum between the slabs in the z direction. During the geometry

optimization, the bottom two layers are fixed while the atomic positions of the adsorbates and the top three layers are relaxed. The Brillouin zone is sampled with a 2 × 3 × 1 Monkhorst–Pack k-point mesh.

The MoP (101) surface is modeled by a 5-layer p(3 × 3) unit cell of 13.5 Å, 9.6 Å with a 20.0 Å vacuum between the slabs in the z direction. During the geometry optimization, the bottom two layers are fixed while the atomic positions of the adsorbates and the top three layers are relaxed. The Brillouin zone is sampled with a 2 × 3 × 1 Monkhorst–Pack k-point mesh.

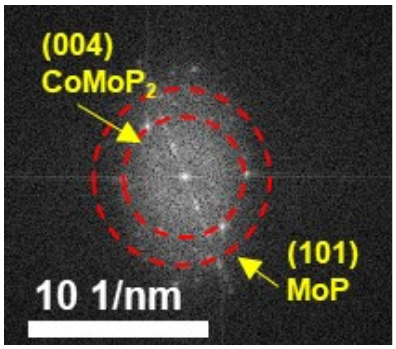

Fig. S1 FFT patterns of MoP/$CoMoP_2$@NPC.

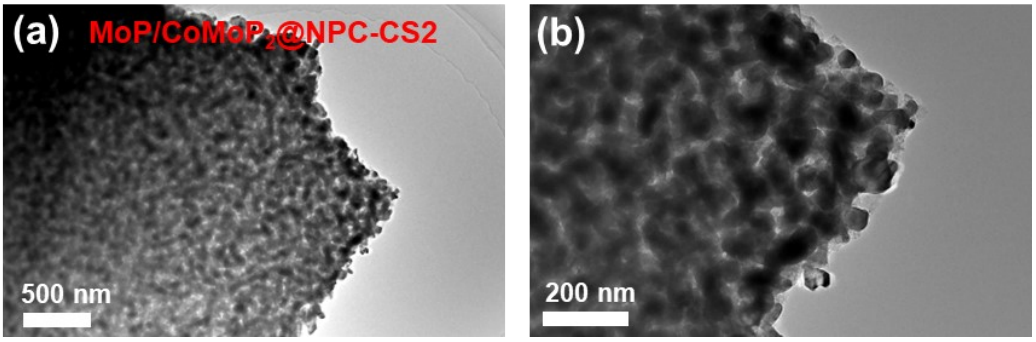

Fig. S2 TEM (a) and HRTEM (b) images of MoP/$CoMoP_2$@NPC-CS2.

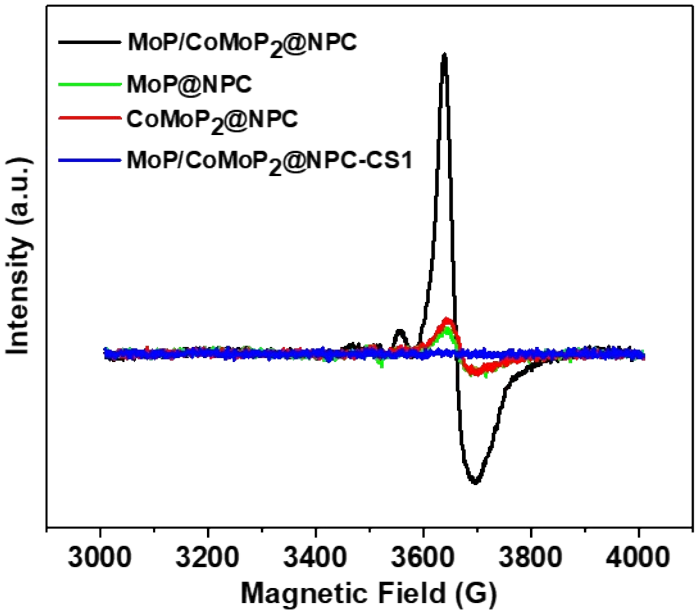

Fig. S3 ESR spectra of MoP@NPC, MoP/$CoMoP_2$@NPC, $CoMoP_2$@NPC and MoP/$CoMoP_2$@NPC-CS1.

Table S1 Binding energies of Mo3d for MoP@NPC, MoP/$CoMoP_2$@NPC and $CoMoP_2$@NPC.

	Mo-P 3d 3/2	Mo-P 3d 5/2	MoO_2 3d 3/2	MoO_2 3d 5/2	MoO_3 3d 3/2	MoO_3 3d 5/2
MoP@NPC	230.7	227.6	232.6	229.1	235.7	232.6
MoP/$CoMoP_2$@NPC	230.9	227.9	231.5	228.8	235.8	232.8
$CoMoP_2$@NPC	231.2	228.2	231.8	229.1	235.9	233.9

Table S2 Binding energies of P2p for MoP@NPC, MoP/$CoMoP_2$@NPC and $CoMoP_2$@NPC.

	P-O	P 2p3/2	P 2p1/2
MoP@NPC	134.0	129.4	130.3
MoP/$CoMoP_2$@NPC	134.2	129.5	130.4
$CoMoP_2$@NPC	134.6	129.2	130.2

Table S3 Binding energies of Co2p for $CoMoP_2$@NPC and MoP/$CoMoP_2$@NPC.

Co2p	CoP 2p 3/2	CoO 2p 3/2	sattlite 2p 3/2	CoP 2p 1/2	CoO 2p 1/2	sattlite 2p 1/2
MoP/$CoMoP_2$@NPC	778.7	781.9	786.4	793.5	797.7	802.9
$CoMoP_2$@NPC	778.2	781.2	785.9	793.0	797.2	802.4

Table S4 Surface atom contents of different elements determined by XPS data for MoP@NPC, MoP/$CoMoP_2$@NPC and $CoMoP_2$@NPC.

	Co	Mo	P	C	O	N
MoP@NPC	0	5.51	8.38	39.46	29.91	16.74
MoP/$CoMoP_2$@NPC	2.69	7.32	4.35	38.13	36.2	11.31
CoMoP2@NPC	5.51	5.37	18.12	32.17	20.13	18.7

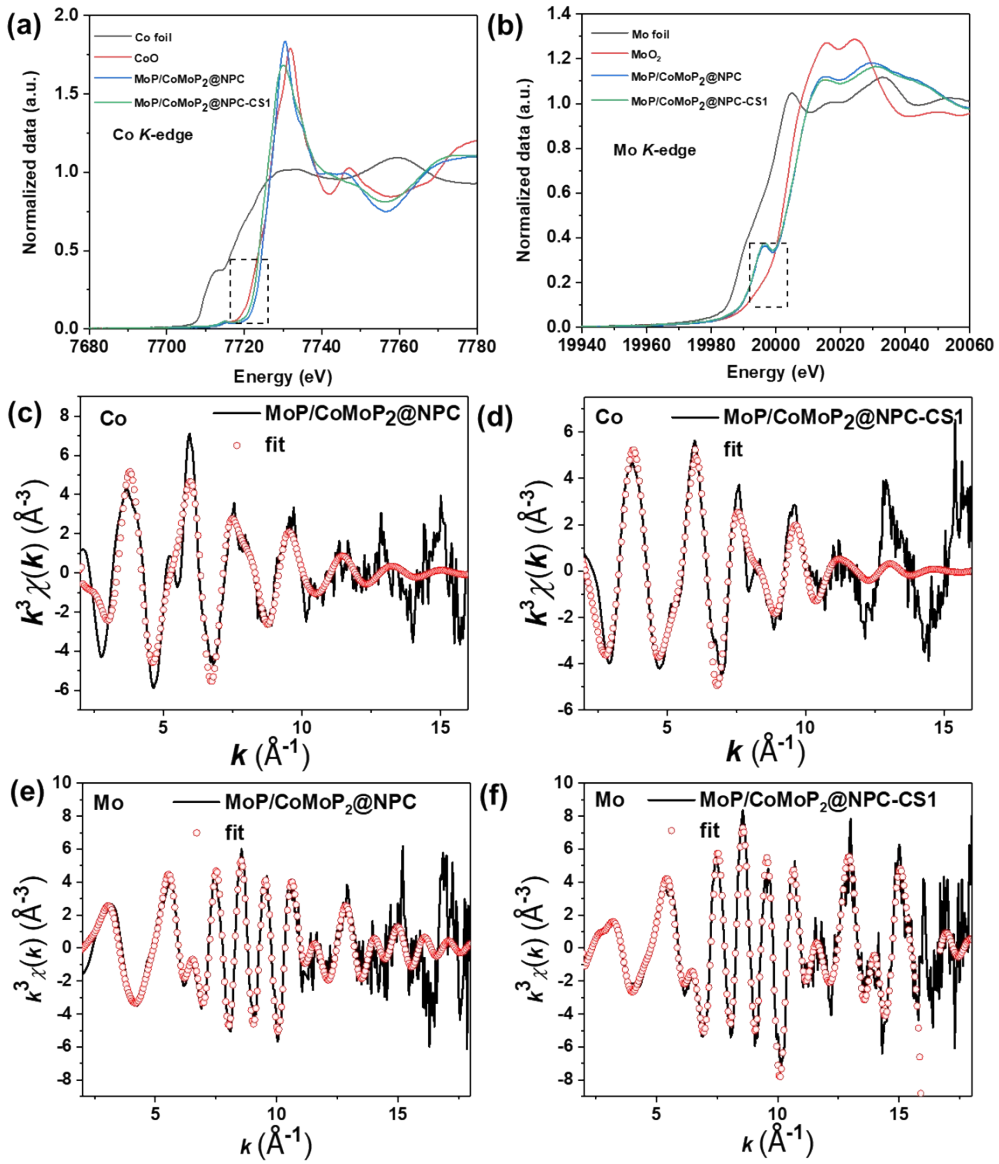

Fig. S4 Co K-edge (a) and Mo K-edge (b) XANES spectra of Co foil, CoO, Mo foil, MoO_2, MoP/CoMoP$_2$@NPC and MoP/CoMoP$_2$@NPC-CS1, respectively. Fourier transforms of the experimental Co K-edge (c, d) and Mo K-edge (e, f) EXAFS spectra of MoP/CoMoP$_2$@NPC and MoP/CoMoP$_2$@NPC-CS1, respectively.

Table S5 EXAFS fitting parameters at the M *K*-edge for various samples.

Sample	Shell	*CN*[a]	*R*(Å)[b]	σ^2(Å^2)[c]	ΔE_0(eV)[d]	*R* factor
Co *K*-edge (S_0^2=0.791)						
Co foil	Co-Co	12*	2.494±0.001	0.0064±0.0001	8.0±0.3	0.0019
MoP/CoMoP$_2$@NPC-CS1	Co-O	**3.9±0.2**	2.088±0.013	0.0119±0.0030	-7.3±1.8	0.0089
	Co-P	**2.2±0.4**	2.236±0.016			
	Co-M	4.4±0.7	3.184±0.013	0.0207±0.0039	9.9±7.7	
MoP/CoMoP$_2$@NPC	Co-O	**5.0±0.2**	2.065±0.023	0.0111±0.0023	-2.3±2.1	0.0037
	Co-P	**0.6±0.1**	2.221±0.016			
	Co-M	2.6±0.3	3.048±0.025	0.0158±0.0052	-1.0±3.3	
Mo *K*-edge (S_0^2=0.946)						
Mo foil	Mo-Mo	8*	2.725±0.003	0.0039±0.0002	-5.9±0.6	0.0058
	Mo-Mo	6*	3.141±0.004	0.0040±0.0003		
MoP/CoMoP$_2$@NPC-CS1	Mo-O	**1.9±0.5**	1.721±0.017	0.0054±0.0012	-1.2±5.5	0.0052
	Mo-P	**1.6±0.3**	2.157±0.020			
	Mo-M	6.7±0.6	3.228±0.021	0.0056±0.0017	4.8±5.0	
	Mo-M	2.7±0.7	3.717±0.018		-0.4±0.2	
MoP/CoMoP$_2$@NPC	Mo-O	**2.7±0.5**	1.702±0.010	0.0032±0.0010	-5.2±5.3	0.0062
	Mo-P	**1.2±0.3**	2.112±0.018			
	Mo-M	4.8±0.8	3.234±0.008	0.0060±0.0008	8.7±1.8	
	Mo-M	3.3±0.6	3.726±0.020		-0.2±4.2	

[a]*CN*, coordination number; [b]*R*, the distance to the neighboring atom; [c]σ^2, the Mean Square Relative Displacement (MSRD); [d]ΔE_0, inner potential correction; *R* factor indicates the goodness of the fit. $S0^2$ was fixed to 0.791 and 0.946, according to the experimental EXAFS fit of Co foil and Mo foil by fixing *CN* as the known crystallographic value. * This value was fixed during EXAFS fitting, based on the known structure of Co and Mo. Fitting range: $3.0 \le k$ (/Å) ≤ 14.9 and $1.0 \le R$ (Å) ≤ 3.0 (Co foil); $3.0 \le k$ (/Å) ≤ 13.5 and $1.0 \le R$ (Å) ≤ 2.4 (Co2); $3.0 \le k$ (/Å) ≤ 11.9 and $1.0 \le R$ (Å) ≤ 2.4 (Co3); $3.0 \le k$ (/Å) ≤ 17.3 and $1.0 \le R$ (Å) ≤ 3.5 (Mo foil); $3.0 \le k$ (/Å) ≤ 15.8 and $1.0 \le R$ (Å) ≤ 2.5 (Mo2); $3.0 \le k$ (/Å) ≤ 15.6 and $1.0 \le R$ (Å) ≤ 2.5 (Mo3). A reasonable range of EXAFS fitting parameters: $0.700 < S_0^2 < 1.000$; $CN > 0$; $\sigma^2 > 0$ Å^2; $|\Delta E_0| < 10$ eV; *R* factor < 0.02.

Table S6 Comparison of HER performance of MoP/$CoMoP_2$@NPC catalysts with other MoP-based electrocatalysts in 0.5 M H_2SO_4.

Electrocatalyst	η_{10} (mV vs.RHE)	Tafel slope (mV dec^{-1})	Reference
MoP/$CoMoP_2$@NPC	**71**	**37**	***This work***
MoP@NC	96	49	[1]
MoP@NPCNFs	64	66	[2]
MoP NA/CC	124	58	[3]
N-MoP/C	150	62	[4]
MoP@C@rGo	169	79	[5]
La-MoP@NC	142	58	[6]
MoP@NPCS	113	58	[7]
MoP@NPC-H	141	59	[8]
MoS_2/MoP/NC	151	58	[9]
MoPS	158	52	[10]
CoP(MoP)-$CoMoO_3$@CN	198	105	[11]
Mo_2C/MoP@NPC	160	75	[12]

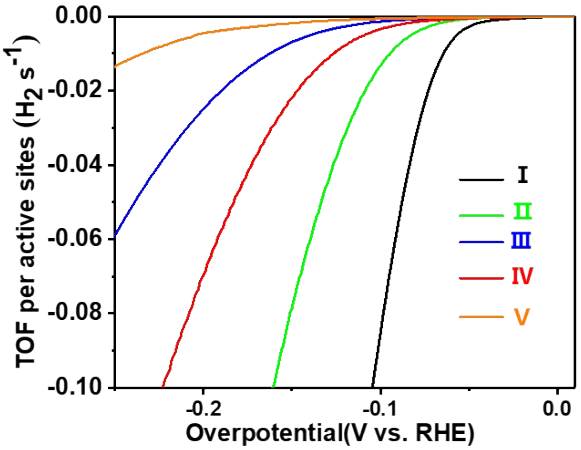

Fig. S5 TOF values for HER in 0.5 M H_2SO_4: I: MoP/$CoMoP_2$@NPC, II: MoP@NPC, III: $CoMoP_2$@NPC, IV: MoP/$CoMoP_2$@NPC @NPC-CS1, V: MoP/$CoMoP_2$@NPC @NPC-CS2.

Table S7 Summarized acidic HER activity of prepared catalysts

Electrocatalyst	**η_{10} (mV vs. RHE)**	**η_{100} (mV vs. RHE)**	**Tafel slope (mV dec^{-1})**	**TOF (100 mV, H_2 s^{-1})**	**TOF (200 mV, H_2 s^{-1})**	**ECSA (cm^2)**	**EIS (Ω)**
MoP@NPC	109	200	61	0.01	0.19	22.2	32.7
$CoMoP_2$@NPC	184	350	96	0.001	0.02	5.4	76.2
MoP/$CoMoP_2$@NPC	71	123	37	0.09	0.60	35.9	13.5
MoP/$CoMoP_2$@NPC-CS1	144	270	84	0.003	0.07	12.9	53.2
MoP/$CoMoP_2$@NPC-CS2	245	413	120	0.0006	0.005	1.7	161.9
Pt/C	34	149	38				

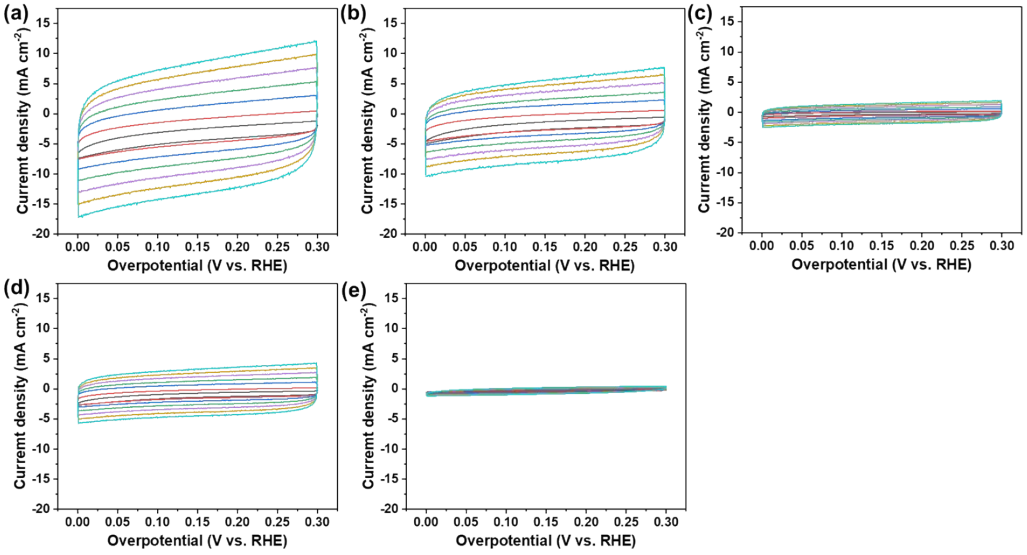

Fig. S6 CV curves with different scan rates in 0.5 M H_2SO_4 for (a) MoP/$CoMoP_2$@NPC, (b) MoP@NPC, (b) $CoMoP_2$@NPC, (d) MoP/$CoMoP_2$@NPC-CS1 and (e) MoP/$CoMoP_2$@NPC-CS2.

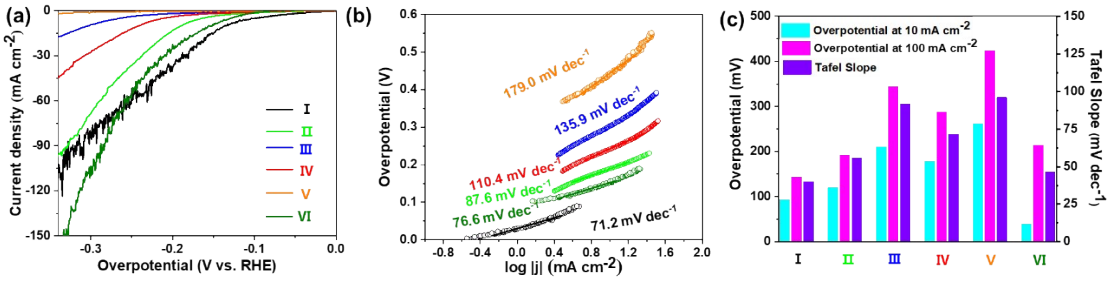

Fig. S7 (a) Polarization curves (iR corrected) for HER in 1 M PBS; (b) their corresponding Tafel plots; (c) Comparisons of η_{10} and Tafel slope of the corresponding samples, I: MoP/$CoMoP_2$@NPC, II: MoP@NPC, III: $CoMoP_2$@NPC, IV: MoP/$CoMoP_2$@NPC @NPC-CS1, V: MoP/$CoMoP_2$@NPC @NPC-CS2, VI: commercial Pt/C.

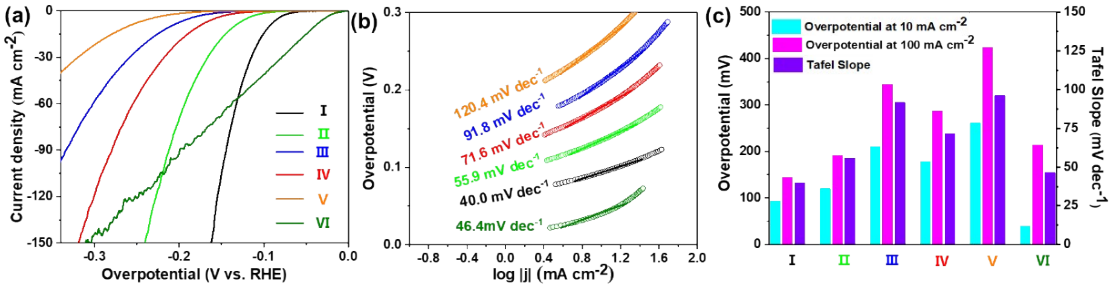

Fig. S8 (a) Polarization curves (iR corrected) for HER in 1 M KOH; (b) their corresponding Tafel plots; (c) Comparisons of η_{10} and Tafel slope of the corresponding samples: I: MoP/$CoMoP_2$@NPC, II: MoP@NPC, III: $CoMoP_2$@NPC, IV: MoP/$CoMoP_2$@NPC @NPC-CS1, V: MoP/$CoMoP_2$@NPC @NPC-CS2, VI: commercial Pt/C.

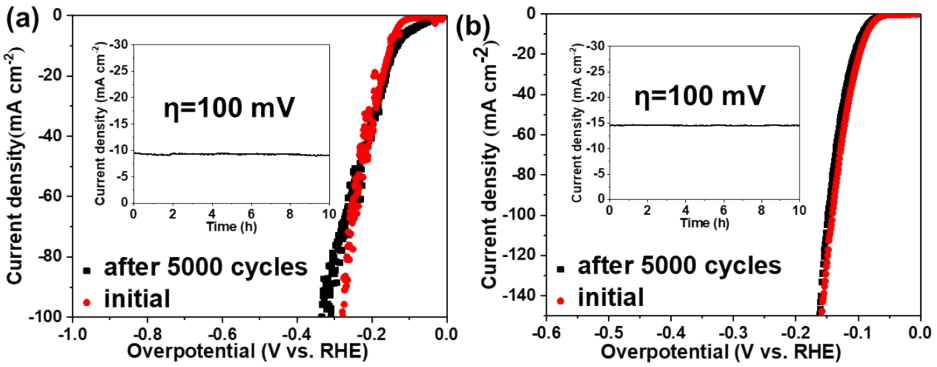

Fig. S9 Stability of the MoP/$CoMoP_2$@NPC with an initial LSV curve and after 5000 cycles in 1 M PBS (a) and 1M KOH (b), inset: the long-term durability tests (CA curve) at η=100 mV.

Table S8 Comparison of HER performance of MoP/$CoMoP_2$@NPC catalysts with other MoP-based electrocatalysts in 1 M PBS and 1 M KOH.

Catalysts	η_{10} (mV) (1 M PBS)	Tafel Slope (mV dec^{-1}) (1 M PBS)	η_{10} (mV) (1 M KOH)	Tafel Slope (mV dec^{-1}) (1 M KOH)	Ref.
MoP/$CoMoP_2$@NPC	**131**	**71**	**93**	**40**	**This work**
MoP NA/CC	187	94	80	83	[3]
MoP@NC	191	95	149	62	[1]
MoP/NPG	150	102	126	56	[13]
P-MoP/Mo_2N	91	51	89	78	[14]
Mo_2C/MoP@NPC	228	125	169	65	[12]
MoP/Mo_2C@C	136	93	75	58	[15]
3.4 at% S-MoP	148	142	106	56	[16]
HF-MoSP	/	456	128	89	[17]
0.02 Ni–MoP	222	160	103	162	[18]

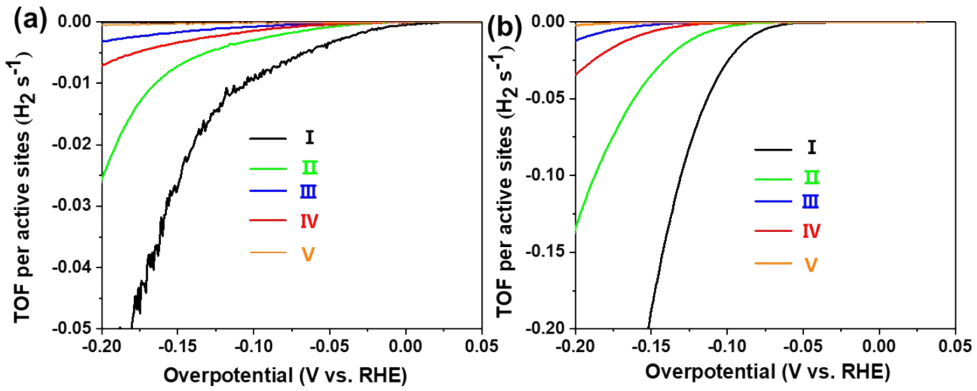

Fig. S10 TOF values of in neutral (a) and alkaline (b) media: I: MoP/$CoMoP_2$@NPC, II: MoP@NPC, III: $CoMoP_2$@NPC, IV: MoP/$CoMoP_2$@NPC @NPC-CS1, V: MoP/$CoMoP_2$@NPC @NPC-CS2.

Table S9 Summarized acidic OER performance of some previously reported electrocatalysis with present work in acidic media.

Catalysts	η_{10} (mV) (0.5 M H_2SO_4)	Tafel Slope (mV dec^{-1}) (0.5 M H_2SO_4)	Ref.
MoP/CoMoP$_2$@NPC	**261**	**37**	**This work**
F doped $Cu_{1.5}Mn_{1.5}O_4$	320	60	[19]
Co_3O_4/FTO	570	80	[20]
Ag-doped Co_3O_4	470	92	[21]
Co_2TiO_4	513	240	[22]
Co_3O_4@C/CP	370	82	[23]
$Co_{0.05}Fe_{0.95}O_y$	650	110	[24]
Fe-TiO_x LNWs/Ti	260	126	[25]
FeNC	320	305	[26]
$MoS_2/Co_9S_8/Ni_3S_2$/Ni	225	78	[27]
SWCNTs/$MoSe_2$-2:Mo_2C	197	/	[28]

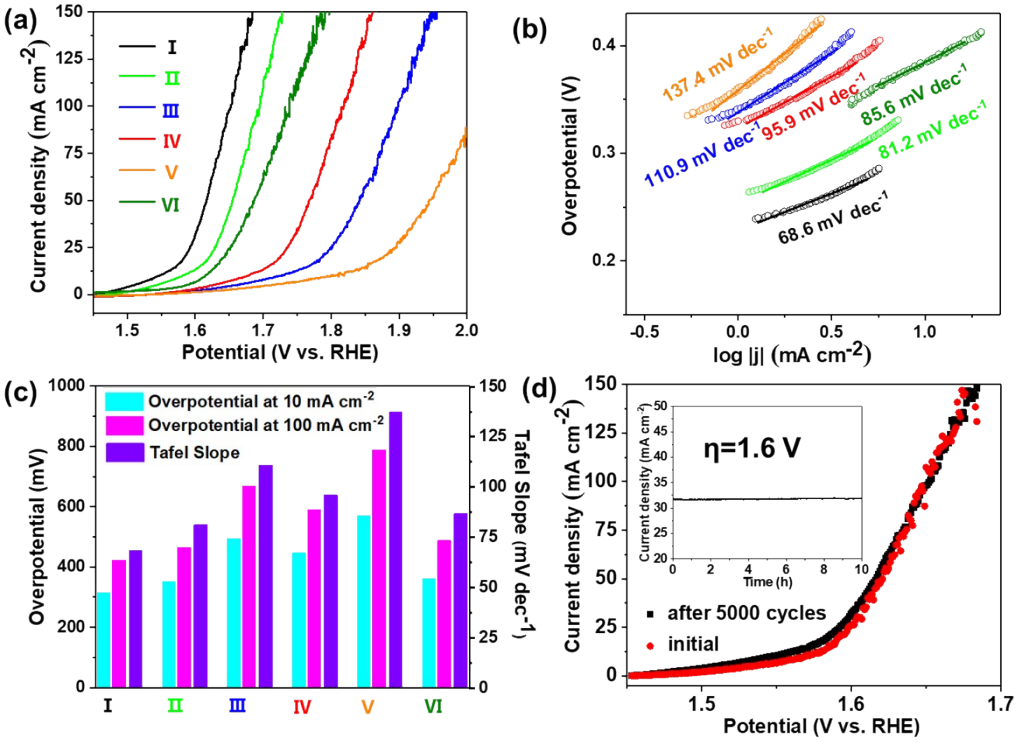

Fig. S11 (a) Polarization curves (iR corrected) for OER in 1 M PBS; (b) their corresponding Tafel plots; (c) Comparisons of η_{10} and Tafel slope of the corresponding samples. (d) Stability of the MoP/$CoMoP_2$@NPC with an initial LSV curve and after 5000 cycles in 0.5 M H_2SO_4, inset: the long-term durability tests (CA curve) at η=1.6 V. I: MoP/$CoMoP_2$@NPC, II: MoP@NPC, III: $CoMoP_2$@NPC, IV: MoP/$CoMoP_2$@NPC @NPC-CS1, V: MoP/$CoMoP_2$@NPC @NPC-CS2, VI: commercial Pt/C.

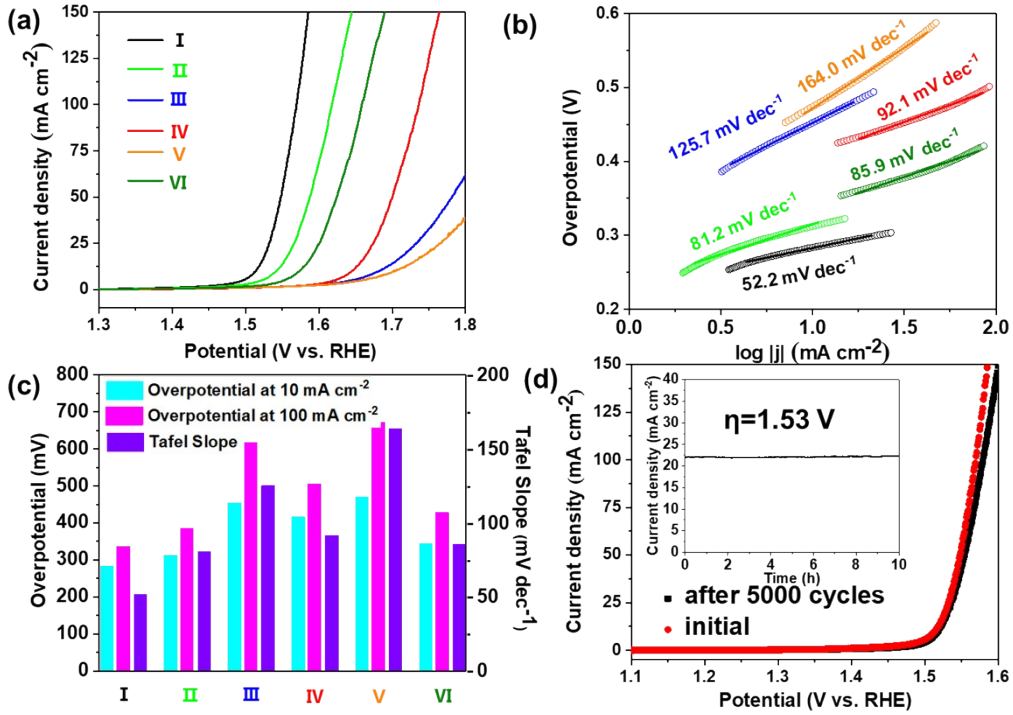

Fig. S12 (a) Polarization curves (iR corrected) for OER in 1 M KOH; (b) their corresponding Tafel plots; (c) Comparisons of η_{10} and Tafel slope of the corresponding samples. (d) Stability of the MoP/$CoMoP_2$@NPC with an initial LSV curve and after 5000 cycles in 0.5 M H_2SO_4, inset: the long-term durability tests (CA curve) at η=1.6 V. I: MoP/$CoMoP_2$@NPC, II: MoP@NPC, III: $CoMoP_2$@NPC, IV: MoP/$CoMoP_2$@NPC @NPC-CS1, V: MoP/$CoMoP_2$@NPC @NPC-CS2, VI: commercial Pt/C.

Table S10 OER parameters in 0.5M H_2SO_4 for MoP@NPC, MoP/$CoMoP_2$@NPC, $CoMoP_2$@NPC, MoP/$CoMoP_2$@NPC-CS1 and MoP/$CoMoP_2$@NPC-CS2.

	η_{10} (mV)	η_{100} (mV)	Tafel Slope (mV dec^{-1})
MoP@NPC	283	373	61
MoP/$CoMoP_2$@NPC	260	323	37
$CoMoP_2$@NPC	430	560	96
MoP/$CoMoP_2$@NPC-CS1	367	479	84
MoP/$CoMoP_2$@NPC-CS2	456	593	120
RuO_2	298	430	38

Table S11 OER parameters in 1M PBS for MoP@NPC, MoP/$CoMoP_2$@NPC, $CoMoP_2$@NPC, MoP/$CoMoP_2$@NPC-CS1 and MoP/$CoMoP_2$@NPC-CS2.

	η_{10} (mV)	η_{100} (mV)	Tafel Slope (mV dec^{-1})
MoP@NPC	352	466	81
MoP/$CoMoP_2$@NPC	317	423	69
$CoMoP_2$@NPC	495	669	111
MoP/$CoMoP_2$@NPC-CS1	447	589	96
MoP/$CoMoP_2$@NPC-CS2	570	791	137
RuO_2	385	509	87

Table S12 OER parameters in 1 M KOH for MoP@NPC, MoP/$CoMoP_2$@NPC, $CoMoP_2$@NPC, MoP/$CoMoP_2$@NPC-CS1 and MoP/$CoMoP_2$@NPC-CS2.

	η_{10} (mV)	η_{100} (mV)	Tafel Slope (mV dec^{-1})
MoP@NPC	313	388	81
MoP/$CoMoP_2$@NPC	284	340	52
$CoMoP_2$@NPC	453	620	126
MoP/$CoMoP_2$@NPC-CS1	415	507	92
MoP/$CoMoP_2$@NPC-CS2	474	674	164
RuO_2	344	429	86

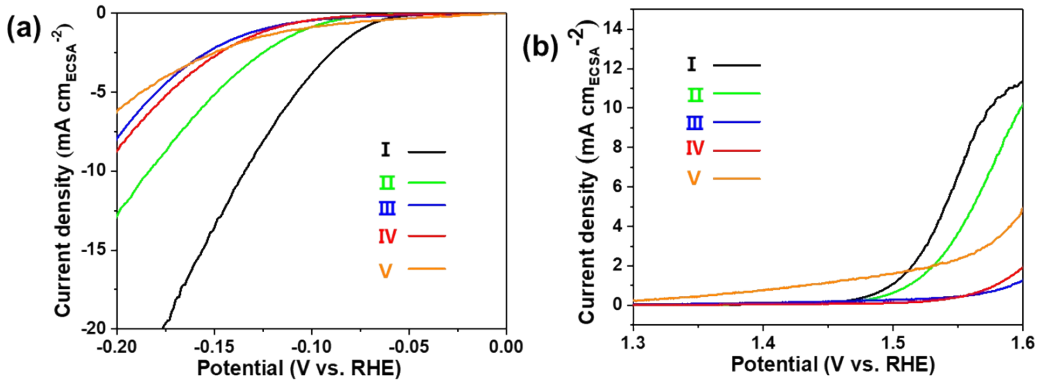

Fig. S13 LSV curves normalized by ECSA for HER and OER in 0.5 M H_2SO_4 of I: MoP/$CoMoP_2$@NPC, II: MoP@NPC, III: $CoMoP_2$@NPC, IV: MoP/$CoMoP_2$@NPC-CS1, V: MoP/$CoMoP_2$@NPC-CS2.

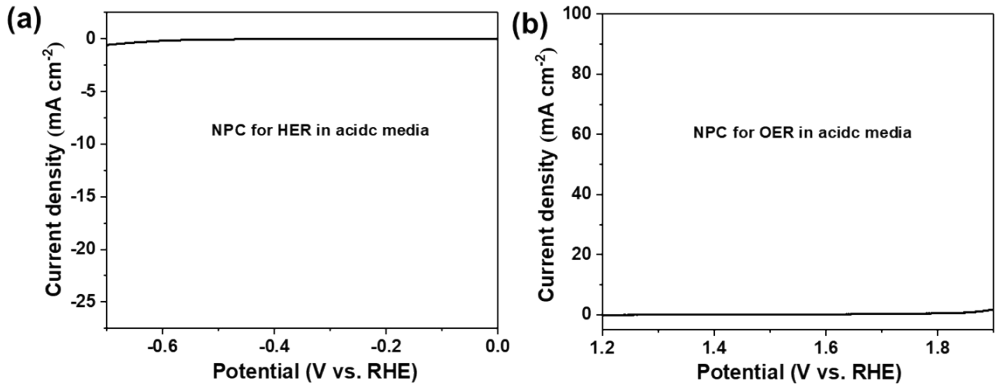

Fig. S14 LSV curves of NPC for HER and OER in acidic media.

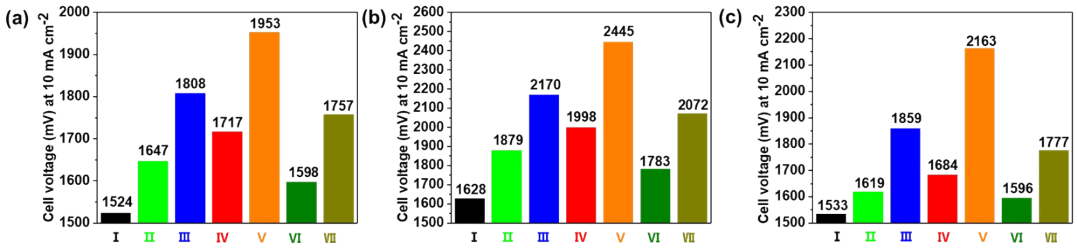

Fig. S15 Comparisons of η_{10} of cell voltage in acidic (a), neutral (b) and alkaline media(c). I: MoP/$CoMoP_2$@NPC||MoP/$CoMoP_2$@NPC, II: MoP@NPC||MoP@NPC, III: $CoMoP_2$@NPC||$CoMoP_2$@NPC, IV: MoP/$CoMoP_2$@NPC-CS1||MoP/$CoMoP_2$@NPC-CS1, V: MoP/$CoMoP_2$@NPC-CS2||MoP/$CoMoP_2$@NPC-CS2, VI: $CoMoP_2$@NPC||MoP@NPC, $CoMoP_2$@NPC||$CoMoP_2$@NP, VII: RuO_2||Pt/C.

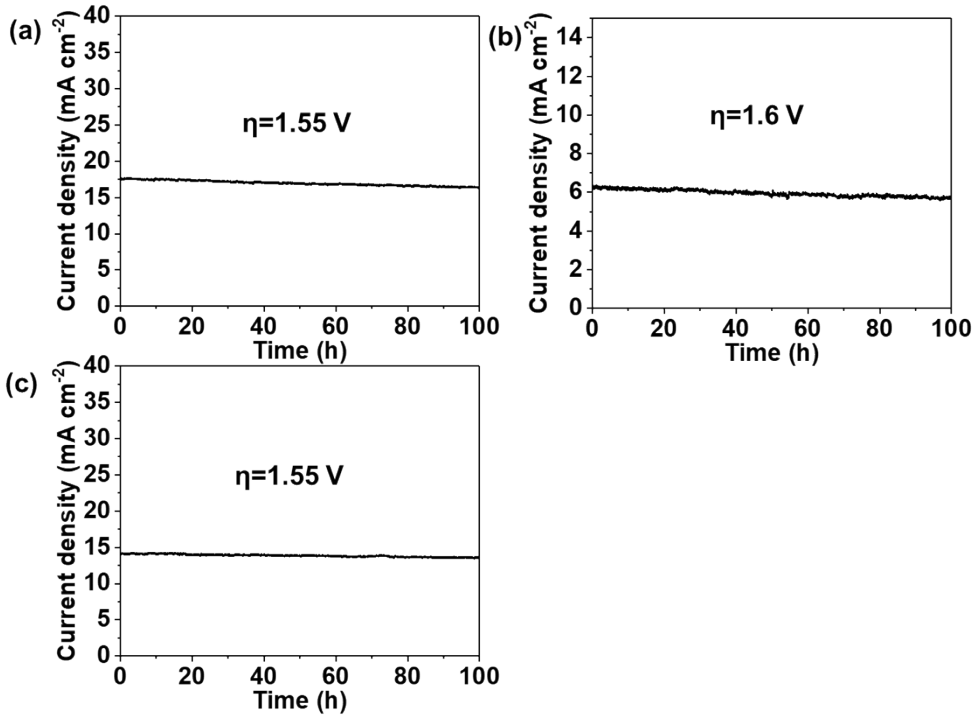

Fig. S16 The long-term durability tests (CA curve) at cell voltage=1.55, 1.6 and 1.55 V in 0.5M H_2SO_4 (a), 1M PBS (b) and 1M KOH (c).

Table S13 Co/Mo/P/C compositions before and after stability test by ICP (Co/Mo) and organic element analysis (P/C).

	Before stability test (%)	After stability test (%)
Co	7.2	6.7
Mo	28.7	25.3
P	12.8	13.2
C	18.5	18.9

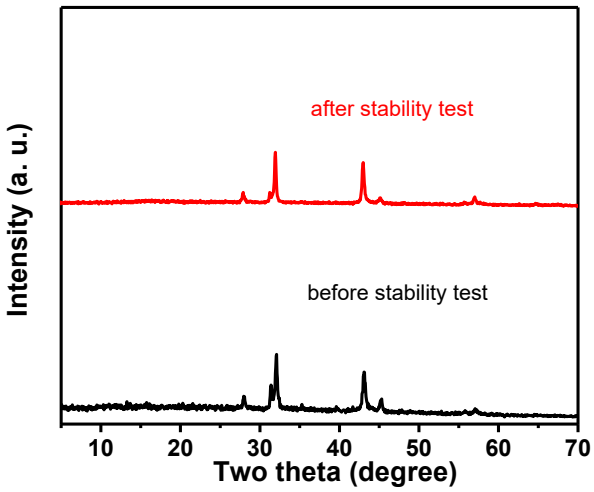

Fig. S17 The XRD patterns of MoP/$CoMoP_2$@NPC before and after stability test.

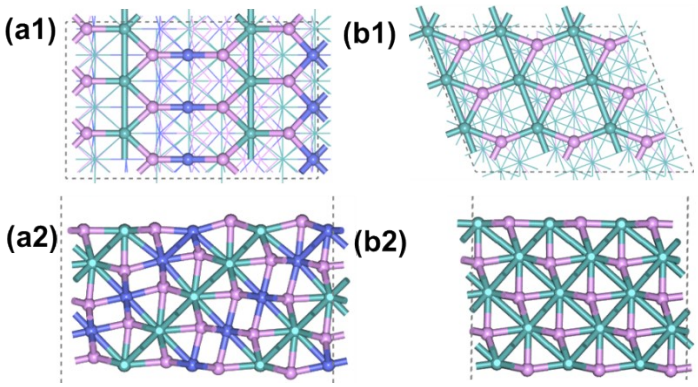

Fig. S18 Top (the first row, 1) and side (the second row, 2) views of (a) $CoMoP_2$(104) and (b) MoP(101) surface. The Mo, Co, P atoms are respectively displayed in cyan , blue and pink.

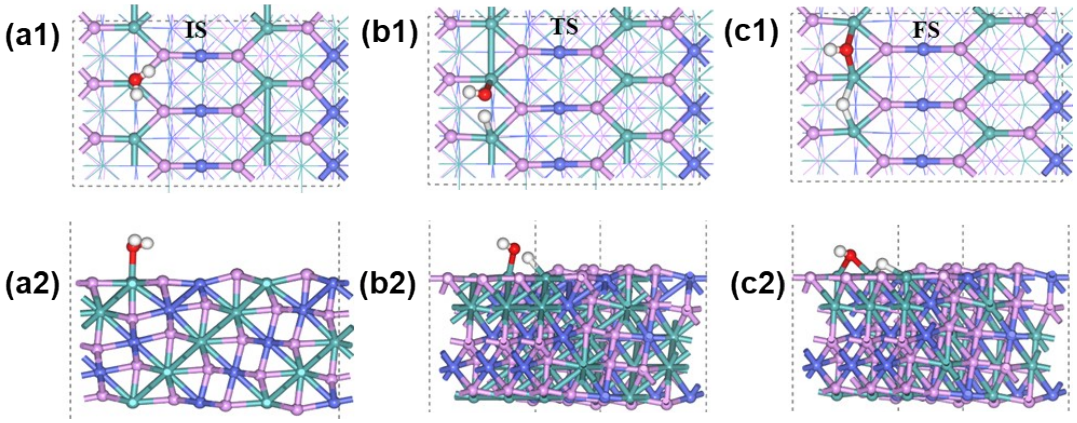

Fig. S19 Top (the first row, 1) and side (the second row, 2) views of DFT optimized IS (a), TS (b) and FS (c) structures for H_2O dissociation on $CoMoP_2$ (104). The H, O atoms are respectively displayed in white and red.

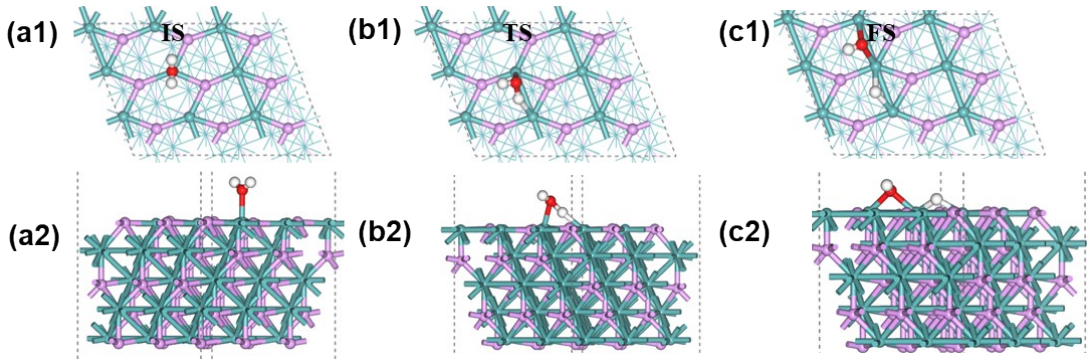

Fig. S20 Top (the first row, 1) and side (the second row, 2) views of DFT optimized IS (a), TS (b) and FS (c) structures for H_2O dissociation on MoP (101).

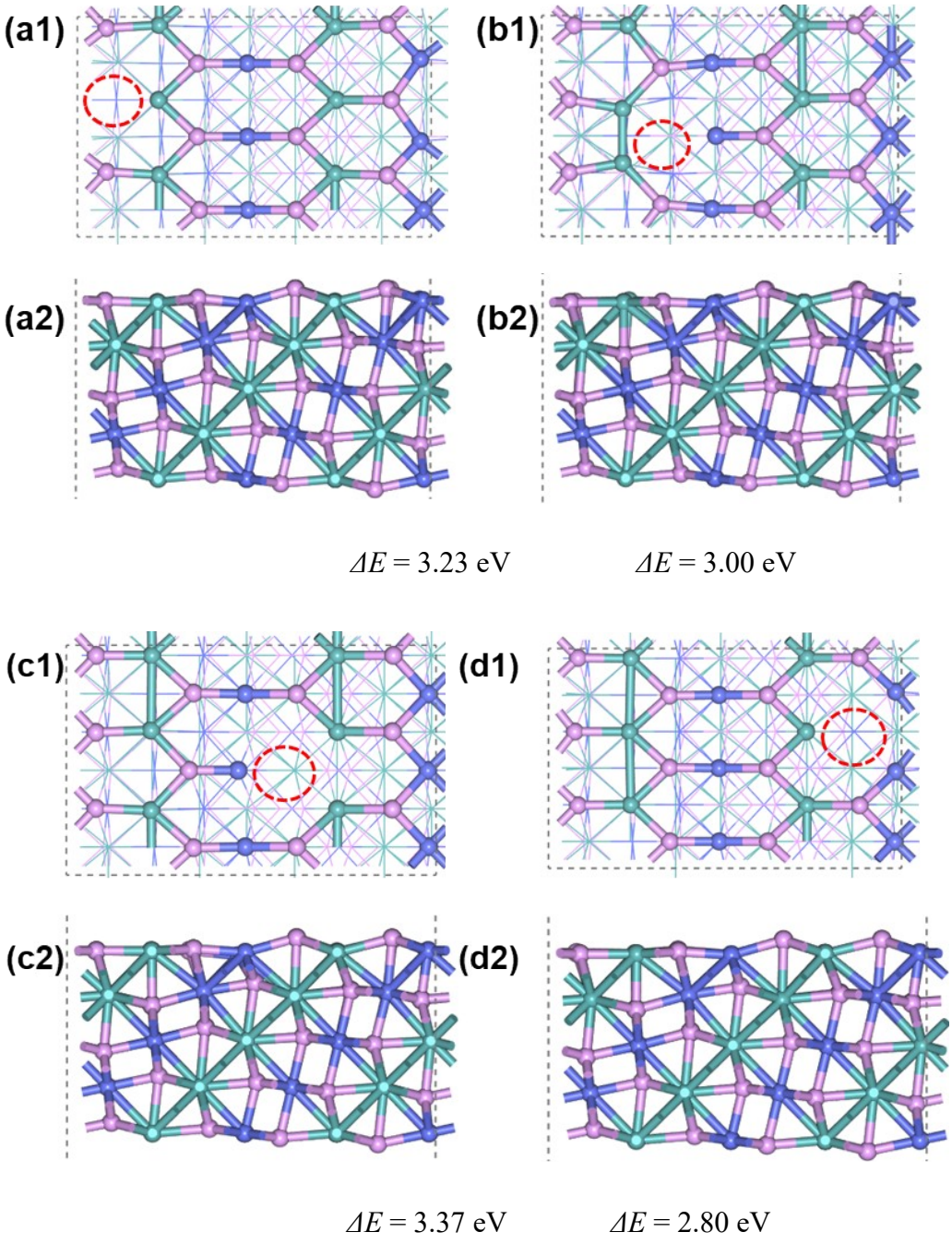

Fig. S21 Top (the first row, 1) and side (the second row, 2) views of possible P vacancy on $CoMoP_2$(104) after geometry optimization (the red dashed circle marks the site of P vacancy) and the reaction energies with reference to the chemical potential of P at gaseous PH_3. The structure shown in Figure S21d2 has the lowest P vacancy formation energy.

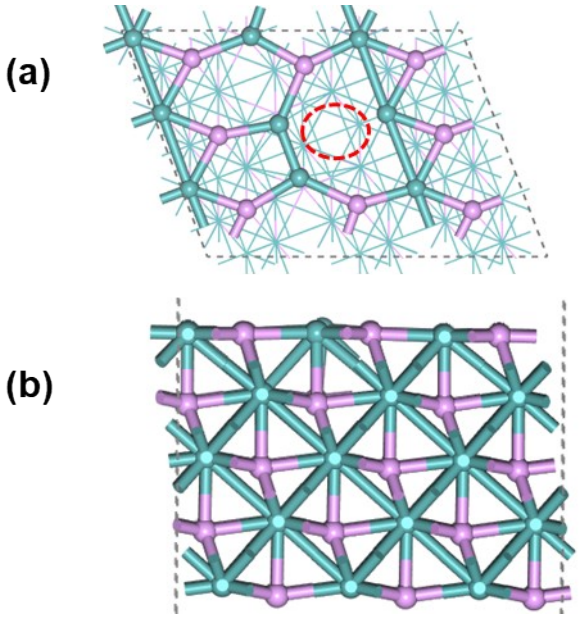

Fig. S22 Top (the first row, a) and side (the second row, b) views of P vacancy on MoP(101) after geometry optimization (the red dashed circle marks the site of P vacancy).

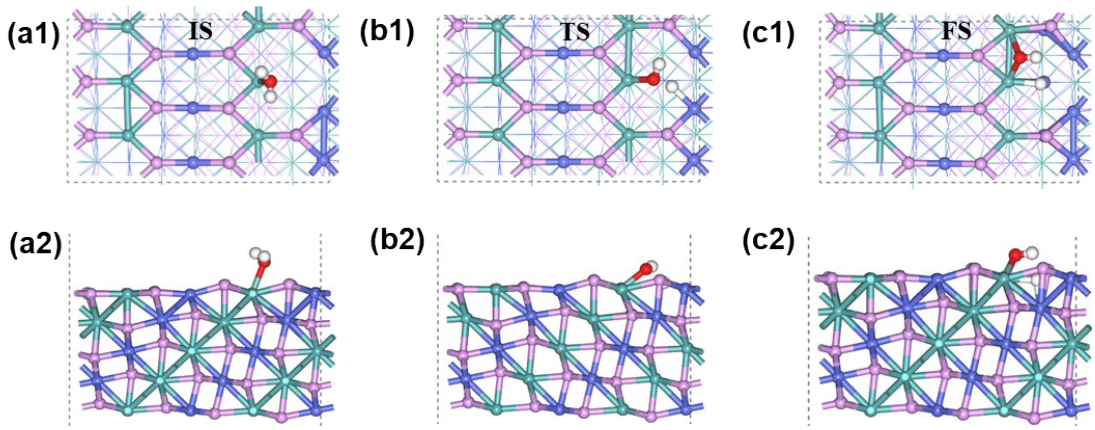

Fig. S23 Top (the first row) and side (the second row) views of DFT optimized IS, TS and FS structures for H_2O dissociation on $CoMoP_2$-Pv.

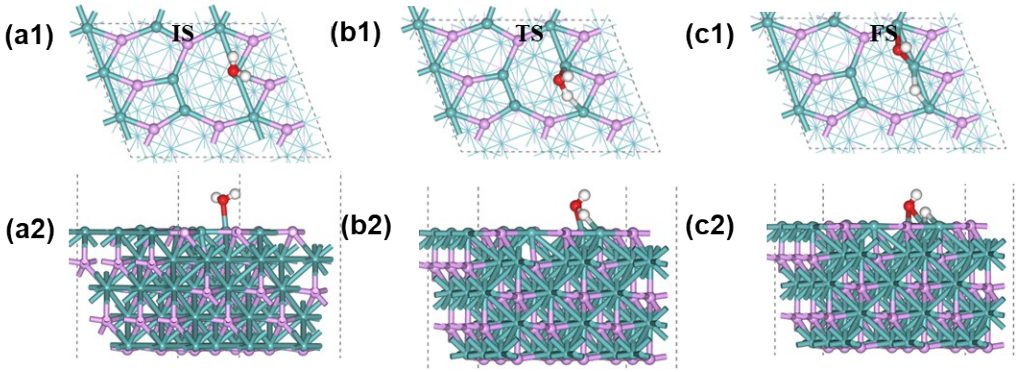

Fig. S24 Top (the first row, 1) and side (the second row, 2) views of DFT optimized IS (a), TS (b) and FS (c) structures for H_2O dissociation on MoP-Pv.

References

1. C. Pi, C. Huang, Y. Yang, H. Song, X. Zhang, Y. Zheng, B. Gao, J. Fu, P. K. Chu and K. Huo, *Applied Catalysis B: Environmental*, 2020, **263**, 118358.
2. M. Wang, C. Ye, M. Xu and S. Bao, *Nano Research*, 2018, **11**, 4728-4734.
3. Z. Pu, S. Wei, Z. Chen and S. Mu, *Applied Catalysis B: Environmental*, 2016, **196**, 193-198.
4. X. Liu, L. Zhang, M. Li and X. Hu, *Chem. Commun. (Cambridge, U. K.)*, 2018, **54**, 2502-2505.
5. Y. Zhang, J. Yang, Q. Dong, H. Geng, Y. Zheng, Y. Liu, W. Wang, C. C. Li and X. Dong, *ACS Appl. Mater. Interfaces*, 2018, **10**, 26258-26263.
6. P. Wei, X. Li, Z. He, Z. Li, X. Zhang, X. Sun, Q. Li, H. Yang, J. Han and Y. Huang, *Applied Catalysis B: Environmental*, 2021, **299**, 120657.
7. J.-T. Ren, L. Chen, D.-D. Yang and Z.-Y. Yuan, *Applied Catalysis B: Environmental*, 2020, **263**, 118352.
8. J.-Q. Chi, W.-K. Gao, L.-M. Zhang, B. Dong, K.-L. Yan, J.-H. Lin, B. Liu, Y.-M. Chai and C.-G. Liu, *ACS Sustainable Chemistry & Engineering*, 2018, **6**, 7676-7686.
9. J.-Q. Chi, Y.-M. Chai, X. Shang, B. Dong, C.-G. Liu, W. Zhang and Z. Jin, *Journal of Materials Chemistry A*, 2018, **6**, 24783-24792.
10. Y. Huang, X. Song, J. Deng, C. Zha, W. Huang, Y. Wu and Y. Li, *Applied Catalysis B: Environmental*, 2019, **245**, 656-661.
11. L. Yu, Y. Xiao, C. Luan, J. Yang, H. Qiao, Y. Wang, X. Zhang, X. Dai, Y. Yang and H. Zhao, *ACS Appl. Mater. Interfaces*, 2019, **11**, 6890-6899.
12. J.-Q. Chi, W.-K. Gao, J.-H. Lin, B. Dong, K.-L. Yan, J.-F. Qin, Z.-Z. Liu, Y.-M. Chai

and C.-G. Liu, *Journal of colloid and interface science*, 2018, **513**, 151-160.

13. R. Ge, J. Huo, T. Liao, Y. Liu, M. Zhu, Y. Li, J. Zhang and W. Li, *Applied Catalysis B: Environmental*, 2020, **260**, 118196.

14. Y. Gu, A. Wu, Y. Jiao, H. Zheng, X. Wang, Y. Xie, L. Wang, C. Tian and H. Fu, *Angew. Chem. Int. Ed.*, 2021, **60**, 6673-6681.

15. L.-N. Zhang, S.-H. Li, H.-Q. Tan, S. U. Khan, Y.-Y. Ma, H.-Y. Zang, Y.-H. Wang and Y.-G. Li, *ACS Appl. Mater. Interfaces*, 2017, **9**, 16270-16279.

16. K. Liang, S. Pakhira, Z. Yang, A. Nijamudheen, L. Ju, M. Wang, C. I. Aguirre-Velez, G. E. Sterbinsky, Y. Du and Z. Feng, *ACS Catalysis*, 2018, **9**, 651-659.

17. A. Wu, C. Tian, H. Yan, Y. Jiao, Q. Yan, G. Yang and H. Fu, *Nanoscale*, 2016, **8**, 11052-11059.

18. M. Ding, H. Xu, M. Liu, Y. Wang, A. Wang, T. Lin, L. Zhang and K. Zhang, *Chem. Eng. J.*, 2022, **430**, 132674.

19. P. P. Patel, M. K. Datta, O. I. Velikokhatnyi, R. Kuruba, K. Damodaran, P. Jampani, B. Gattu, P. M. Shanthi, S. S. Damle and P. N. Kumta, *Scientific reports*, 2016, **6**, 28367.

20. J. S. Mondschein, J. F. Callejas, C. G. Read, J. Y. Chen, C. F. Holder, C. K. Badding and R. E. Schaak, *Chem. Mater.*, 2017, **29**, 950-957.

21. K.-L. Yan, J.-F. Qin, J.-H. Lin, B. Dong, J.-Q. Chi, Z.-Z. Liu, F.-N. Dai, Y.-M. Chai and C.-G. Liu, *Journal of Materials Chemistry A*, 2018, **6**, 5678-5686.

22. S. Anantharaj, K. Karthick and S. Kundu, *Inorg. Chem.*, 2019, **58**, 8570-8576.

23. J. Wang, J. Liu, B. Zhang, H. Wan, Z. Li, X. Ji, K. Xu, C. Chen, D. Zha and L. Miao,

Nano Energy, 2017, **42**, 98-105.

24. W. L. Kwong, C. C. Lee, A. Shchukarev and J. Messinger, *Chem. Commun. (Cambridge, U. K.)*, 2019, **55**, 5017-5020.

25. L. Zhao, Q. Cao, A. Wang, J. Duan, W. Zhou, Y. Sang and H. Liu, *Nano Energy*, 2018, **45**, 118-126.

26. K. Mamtani, D. Jain, A. C. Co and U. S. Ozkan, *Energy Fuels*, 2017, **31**, 6541-6547.

27. Y. Yang, H. Yao, Z. Yu, S. M. Islam, H. He, M. Yuan, Y. Yue, K. Xu, W. Hao and G. Sun, *Journal of the American Chemical Society*, 2019, **141**, 10417-10430.

28. L. Najafi, S. Bellani, R. Oropesa-Nuñez, M. Prato, B. Martín-García, R. Brescia and F. Bonaccorso, *ACS Nano*, 2019, **13**, 3162-3176.